

3-1-2006

Effective heights and tangential momentum accommodation coefficients of gaseous slip flows in deep reactive ion etching rectangular microchannels

Jaesung Jang
Purdue University

Steven Wereley
Birck Nanotechnology Center, Purdue University, wereley@purdue.edu

Follow this and additional works at: <http://docs.lib.purdue.edu/nanodocs>

Jang, Jaesung and Wereley, Steven, "Effective heights and tangential momentum accommodation coefficients of gaseous slip flows in deep reactive ion etching rectangular microchannels" (2006). *Other Nanotechnology Publications*. Paper 52.
<http://docs.lib.purdue.edu/nanodocs/52>

This document has been made available through Purdue e-Pubs, a service of the Purdue University Libraries. Please contact epubs@purdue.edu for additional information.

Effective heights and tangential momentum accommodation coefficients of gaseous slip flows in deep reactive ion etching rectangular microchannels

Jaesung Jang¹ and Steven T Wereley²

¹ Laboratory of Integrated Biomedical Micro/Nanotechnology and Applications, Birck Nanotechnology Center, School of Electrical and Computer Engineering, Purdue University, West Lafayette IN 47907, USA

² Microfluidics Laboratory, School of Mechanical Engineering, Purdue University, West Lafayette, IN 47907, USA

E-mail: wereley@purdue.edu

Received 7 December 2005

Published 30 January 2006

Online at stacks.iop.org/JMM/16/493

Abstract

The behavior of a rarefied, compressible flow in long, constant cross section channels provides an opportunity to study complex gas dynamics in a simple geometry that allows analytical solutions. The problem of a rarefied, compressible flow in near unity aspect ratio rectangular cross section channels has been all but ignored despite it being a common flow geometry. We present analytical expressions for the mass flow rate in long, straight and uniform rectangular cross section microchannels in the slip flow regime. Using these analytical expressions, we extract the tangential momentum accommodation coefficient (TMAC) as well as the effective channel dimensions to account for a slight curvature of one of the walls of the rectangle. These expressions are effective in near unity aspect ratio rectangular microchannels made by deep reactive ion etching. The dependence of the flow behavior on the channel height to width aspect ratio is discussed as is the effect of the slight deviation from a rectangular cross section. The obtained TMAC results are consistent with values found by previous researchers using similar materials. Finally, a method of determining TMACs in channels consisting of non-homogenous materials or processing methods is presented.

Nomenclature

a	channel aspect ratio h/w_c	n^o	coordinate in the outward normal direction from the wall
D_h	hydraulic diameter of a noncircular channel (m)	p	pressure (Pa)
H	channel height (m)	p_c	characteristic pressure $(2L/h)(\mu v_{o,avg})/H$ (Pa)
h	channel half height (m)	R_s	specific gas constant (J (kg K) ⁻¹)
Kn	Knudsen number λ/H	Re	Reynolds number $(\rho_o v_{o,avg} H)/\mu$
\overline{Kn}	modified Knudsen number $Kn(2 - \sigma)/\sigma$	Re_{D_h}	Reynolds number based on the hydraulic diameter $(\rho_o v_{o,avg} D_h)/\mu$
L	channel length between upstream and downstream of interests (m)	s^t	coordinate in the tangential streamwise direction on the wall
\dot{m}	mass flow rate (kg s ⁻¹)	T	temperature (K)
		t	time (s)

\underline{u}	velocity vector
v	streamwise velocity (m s ⁻¹)
\bar{v}	streamwise velocity component nondimensionalized with $(h^2/\mu)(dp/dz)$
v_s	gas velocity at the wall (m s ⁻¹)
w_c	channel half width (m)
x	widthwise coordinate
y	depthwise coordinate
z	streamwise coordinate

Greek symbols

η	dimensionless variable for the y direction y/h
κ	eigenvalue
λ	mean free path of a gas (m)
μ	dynamic viscosity (kg (m s) ⁻¹)
ζ	dimensionless variable for the x direction x/w_c
Π	pressure ratio p_i/p_o
ρ	density (kg m ⁻³)
σ	tangential momentum accommodation coefficient
σ_S	standard deviation

Subscripts

avg	average
comp	compressible
i	inlet or upstream
ns	no slip
o	outlet or downstream
s	slip
w	wall

1. Introduction

During the past few decades, rapid developments in micromachining technologies have made it possible to fabricate micron-sized mechanical systems, the most prototypical of which are microchannels. The microchannel is one of the simplest and most common components in microfluidic and micro heat transfer systems. However, flows at microscopic length scales differ from those at macroscopic length scales for several reasons. In microscale liquid flows, wetting, electrokinetics and adsorption become important while rarefaction, compressibility and velocity slip at boundaries must be considered in microscale gas flows [1].

The Knudsen number (Kn) is defined as the ratio of the mean free path of a gas to the characteristic length scale of a flow and it is used to quantify non-continuum effects. The flow is said to be in the continuum flow regime if $Kn < 10^{-3}$, while the flow is said to be in the slip flow regime if $10^{-3} < Kn < 10^{-1}$. This classification is based on empirical observation. In microchannel gas flows, the characteristic length scale of the flow is oftentimes in the range of microns or tens of microns, while the molecular mean free path is approximately 65 nm at atmospheric conditions. Consequently, gas flows in microchannels are often in the slip flow regime. In this regime, analyses based on the Navier–Stokes equation with slip boundary conditions have been successful [2–4]. In these cases, a discrete velocity slip region exists at the interfaces while the interior of the flow behaves as a continuum [5]. Although rarefied gas dynamics has received considerable attention since the 1960s, the applications have largely been restricted to low pressure

vacuum processes and space vehicles. Recent advances in micromachining technologies and the resulting diminution of length scales have made rarefied gas dynamics important at atmospheric pressure levels in a wider variety of geometries.

Velocity slip at gas–solid interfaces was first proposed by Kundt and Warburg in 1875 [6, 7]. They found that when a disk oscillates in a low pressure gas at constant temperature, the decay of the oscillation amplitude of the disk is slower than that predicted by continuum viscous drag models. They proposed that the decrease in viscous damping is due to the flow slipping at the gas–solid interfaces. Later Maxwell provided a theoretical basis for velocity slip using kinetic gas theory [8]. The first-order velocity slip boundary condition in the slip flow regime can be expressed by [1]

$$v_s = \frac{2 - \sigma}{\sigma} \lambda \left. \frac{\partial v}{\partial n^o} \right|_w + \frac{3}{4} \frac{\mu}{\rho T} \left. \frac{\partial T}{\partial s^t} \right|_w. \quad (1)$$

The first term is related to the wall shear stress and the second term is associated with thermal creep, which is important in channels having a tangential temperature gradient. For isothermal channels, the second term in equation (1) is zero. The assumption of isothermal flow is good for low Mach number flows in long non-insulated microchannels and has been used in many micro flow analyses [2, 4, 9, 10].

The tangential momentum accommodation coefficient (TMAC), σ , is an important parameter in determining the degree of the slip and represents the average tangential momentum exchange between the flowing gas molecules and the solid boundary [1]. The TMAC is a unique parameter that combines surface physics (gas type and boundary material) with the mechanical properties of the surface finish. The case of $\sigma = 0$ is called *specular reflection*, meaning zero skin friction. The case of $\sigma = 1$ is called *diffuse reflection*. In this case, the molecules are reflected with zero average tangential velocity, a good model for rough surfaces.

To date, several gas flow experiments in microchannels and micro ducts have been published demonstrating this slip phenomenon in various simple geometries [5]. Pfahler *et al* [11] and Harley *et al* [2] presented some of the first analytical and experimental works on rarefied flows in micro-fabricated channels at atmospheric conditions. They demonstrated that slip flow exists in micromachined channels. Pong *et al* [10] and Liu *et al* [12] presented the first experimental measurements of pressure distributions along microchannels using an array of surface micromachined piezoresistive pressure sensors. They showed that nonlinear pressure distributions exist in the microchannels due to compressibility. Shih *et al* [13] presented mass flow measurements and pressure distributions for this apparatus. Their measurements were not consistent with any theory [3]. Arkilic *et al* [9] presented a two-velocity component analysis of flow in planar microchannels using the Navier–Stokes equations with a first-order slip-velocity boundary condition. However, the pressure distribution, a very important parameter for understanding microflows, was not measured.

Lee *et al* [14] and Li *et al* [15] developed more complex gas flow systems involving bends, sharp corners and orifices. They assumed the TMAC to be unity in their calculation of mass flow rates and pressure distributions within the microchannel networks. Although TMAC is not necessarily

unity in microchannels [1], it is a reasonable choice for many gas–surface interactions when the appropriate value is unavailable [3]. Colin *et al* [16] experimentally found that a rectangular model should be taken into account even in channels with an aspect ratio as small as 0.087. Their channels were produced using the deep reactive ion etching (DRIE) process. DRIE is a popular and attractive process due to its ability to etch silicon trenches a few hundred microns deep, as small as single microns wide, with nearly vertical walls [17]. Such geometries are very difficult to make with other microfabrication techniques. This process causes slightly curved channel bottom surfaces due to the isotropic etching cycles [17]. Colin *et al* [16] did not consider the effect of boundary curvature on mass flow.

The present work differs from previous microchannel gas flow experiments in that near unity aspect ratio rectangular channels will be used here whereas previous works have generally used thin, wide, effectively planar channels [18]. Further, the effect of a curved channel bottom surface due to the DRIE process on the mass flow has never been addressed. This effect needs to be considered carefully because calculating mass flow rate from the measured pressure drop is very sensitive to channel size measurements. Arkilic *et al* [19] presented a method to extract effective heights and TMACs in planar microchannels from flow measurements. There have been several numerical studies of slip flow for particular aspect ratio rectangular microchannels [1, 20–22], but the formula with which it is possible to extract effective channel heights and TMACs of a general rectangular microchannel has not been developed in the slip flow regime. That is, this work will extend [19] to rectangular microchannels. In this work, we will present analytical mass flow rate expressions in a rectangular microchannel, and measure effective heights and TMACs of a gas flowing in a rectangular microchannel fabricated using DRIE from those expressions. Finally, the effect of a slight departure from a rectangular cross section (in this case a curved bottom wall) will be discussed.

2. Theoretical backgrounds

When deriving the governing equations for the flow, it is assumed that the flow in the rectangular microchannel is steady state, two-dimensional and isothermal with negligible transverse velocities. The inertia effects in the momentum equations can be neglected for a relatively low Reynolds number flow in long microchannels, i.e. those with a large ratio of channel length to height [1, 2, 4]. Under these assumptions, the flow is not necessarily incompressible because large-pressure drops can be produced by viscous dissipation in the microchannel even at Mach numbers much less than 0.3 [1, 5]. In the absence of inertial effects, the flow can be treated as locally fully developed where the velocity field at any cross section is the same as that of a fully developed flow at the local density [23].

The Navier–Stokes equation for a compressible flow is given by

$$\frac{\partial(\rho \underline{u})}{\partial t} + \nabla \cdot (\rho \underline{u} \underline{u}) = -\nabla p + \mu \nabla^2 \underline{u} + \frac{1}{3} \mu \nabla (\nabla \cdot \underline{u}). \quad (2)$$

If equation (2) is nondimensionalized for the assumption of steady state and negligible transverse velocities in the x (width) and y (height) directions, the streamwise momentum equation (the z direction) can be expressed as

$$\left(\frac{h}{2L}\right) \cdot Re \frac{\partial}{\partial z^*} (\rho^* v^{*2}) = -\frac{\partial p^*}{\partial z^*} + \left(\frac{h}{w_c}\right)^2 \frac{\partial^2 v^*}{\partial x^{*2}} + \frac{\partial^2 v^*}{\partial y^{*2}} + \frac{4}{3} \left(\frac{h}{L}\right)^2 \frac{\partial^2 v^*}{\partial z^{*2}}, \quad (3)$$

where the superscript $*$ represents nondimensionalization of variables. When the product of the Reynolds number and the height to length ratio is negligible, the resulting equation is one where the pressure gradient term is counterbalanced by x and y directional viscous terms. This could be considered as the first term in a perturbation expansion of equation (3) [4]. The simplified governing equation is given by

$$\frac{\partial^2 v}{\partial x^2} + \frac{\partial^2 v}{\partial y^2} = \frac{1}{\mu} \frac{dp}{dz}. \quad (4)$$

The first-order velocity slip boundary conditions and symmetry conditions are given by

$$x = 0, \quad 0 \leq y \leq h \quad \frac{\partial v}{\partial x} = 0 \quad (5a)$$

$$x = w_c, \quad 0 \leq y < h \quad v = -\frac{2-\sigma}{\sigma} \lambda \frac{\partial v}{\partial x} \quad (5b)$$

$$y = 0, \quad 0 \leq x \leq w_c \quad \frac{\partial v}{\partial y} = 0 \quad (5c)$$

$$y = h, \quad 0 \leq x < w_c \quad v = -\frac{2-\sigma}{\sigma} \lambda \frac{\partial v}{\partial y}. \quad (5d)$$

Ebert and Sparrow [23] presented the dimensionless velocity in rectangular channels in the slip flow regime assuming constant fluid properties and fully developed flow conditions, neither of which has been assumed in the current derivation. However, their governing equation and boundary conditions were identical to those given in equations (4) and (5). Hence their solution can be used with our locally fully developed assumption, provided the pressure gradient does not vary significantly along the channel, which is assured when the inertia terms in equation (3) are negligible. The dimensionless velocity, which was obtained by solving an eigenvalue problem, is given by

$$\bar{v}(\xi, \eta) = \sum_n \frac{2 \sin \kappa_n}{\kappa_n^3} \left(\frac{1}{1 + 2\overline{Kn} \sin^2 \kappa_n} \right) \times \left(\frac{\cosh\left(\frac{\kappa_n \xi}{a}\right)}{\cosh\left(\frac{\kappa_n}{a}\right) + 2\kappa_n \overline{Kn} \sinh\left(\frac{\kappa_n}{a}\right)} - 1 \right) \cos \kappa_n \eta. \quad (6)$$

The characteristic equation for determining the eigenvalues is

$$\kappa \tan \kappa = 1/(2\overline{Kn}), \quad (7)$$

where $\kappa = 0$ produces a trivial solution.

2.1. Eigenvalues at a slightly rarefied flow

In order to separate continuum and sub-continuum effects and to extract the TMAC and effective height of the microchannel, it is necessary to arrange equation (6) in a power series of \overline{Kn} as

$$\bar{v}(\xi, \eta) = \sum (C_1 + C_2 \overline{Kn} + C_3 \overline{Kn}^2 + \dots), \quad (8)$$

Table 1. The validation of the approximation of ε_n . The values of ε_n obtained from the characteristic equation of $\kappa \tan \kappa = 1/(2\overline{Kn})$ at $\overline{Kn} = 0.001$ are compared with the approximation of $n\pi \overline{Kn}$.

n	Eigenvalues	$n/2$	ε_n	$n\pi \overline{Kn}$	% Difference
1	1.567 66	0.5	0.003 14	0.003 14	0.00
3	4.702 98	1.5	0.009 41	0.009 42	0.11
5	7.838 31	2.5	0.015 68	0.015 71	0.19
7	10.973 63	3.5	0.021 94	0.021 99	0.23
9	14.108 96	4.5	0.028 21	0.028 27	0.21
11	17.244 28	5.5	0.034 47	0.034 56	0.26
13	20.379 62	6.5	0.040 74	0.040 84	0.25
15	23.514 95	7.5	0.047 00	0.047 12	0.26
17	26.650 29	8.5	0.053 25	0.053 41	0.30
19	29.785 63	9.5	0.059 5	0.059 69	0.32
21	32.920 98	10.5	0.065 75	0.065 97	0.33
23	36.056 33	11.5	0.071 99	0.072 26	0.38
25	39.191 68	12.5	0.078 22	0.078 54	0.41
27	42.327 05	13.5	0.084 45	0.084 82	0.44
29	45.462 42	14.5	0.090 68	0.091 11	0.47
31	48.597 79	15.5	0.096 89	0.097 39	0.52

where $C1$, $C2$ and $C3$ are not functions of \overline{Kn} . Further, the eigenvalues are functions of the Knudsen number, so to fully separate continuum and sub-continuum effects it is also necessary to construct a similar power series in the Knudsen number for the eigenvalues. The eigenvalues at small Knudsen numbers can be represented by

$$\kappa_n = \frac{n\pi}{2} - \varepsilon_n, \quad n = 1, 3, 5, 7, \dots, \quad (9)$$

where ε_n are small values much less than unity and a function of the modified Knudsen number. If we substitute equation (9) into the characteristic equation and use a trigonometric identity, L'Hôpital's rule, and a small angle approximation to simplify the expression, we find ε_n as

$$\varepsilon_n = n\pi \overline{Kn}. \quad (10)$$

The accuracy of this approximation can be assessed by comparing to the exact values determined from the characteristic equation for several values of n , which is shown in table 1. The differences between the approximations and the analytical values are very small. The relative error at the largest n shown in table 1 is 0.52%. The eigenvalues can then be expressed by

$$\kappa_n = \frac{n\pi}{2} - n\pi \overline{Kn}, \quad n = 1, 3, 5, 7, \dots \quad (11)$$

2.2. Mass flow rate

Using a Taylor series expansion about $n\pi/2$ (eigenvalues at a Knudsen number of zero or continuum), the mass flow rate can be obtained by applying the ideal gas law and the relationship between pressure and the local Knudsen number at isothermal conditions, $p(z)Kn(z) = p_o Kn_o$, and then integrating over

the cross section to find

$$\begin{aligned} \dot{m} &= \frac{w_c h^3}{R_s T \mu} \int_{-1}^1 \int_{-1}^1 p \frac{dp}{dz} \overline{v}(\xi, \eta) d\xi d\eta = \frac{w_c h^3}{R_s T \mu} p \frac{dp}{dz} \text{CP1} \\ &+ \frac{w_c h^3}{R_s T \mu} \frac{dp}{dz} \frac{2-\sigma}{\sigma} Kn_o p_o \text{CP2}. \end{aligned} \quad (12)$$

CP1 and CP2 are represented as

$$\text{CP1} = -\frac{4}{3} \left(1 - \frac{192}{\pi^5} \left(\frac{h}{w_c} \right) \sum_{n=1,3,5,\dots}^{\infty} \frac{1}{n^5} \tanh \left(\frac{n\pi}{2} \frac{w_c}{h} \right) \right) \quad (13a)$$

and

$$\begin{aligned} \text{CP2} &= -\frac{32}{3} \left(1 - \frac{192}{\pi^5} \left(\frac{h}{w_c} \right) \sum_{n=1,3,5,\dots}^{\infty} \frac{1}{n^5} \tanh \left(\frac{n\pi}{2} \frac{w_c}{h} \right) \right) \\ &+ \frac{256}{\pi^4} \left(1 - \frac{h}{w_c} \right) \sum_{n=1,3,5,\dots}^{\infty} \frac{1}{n^4} \tanh^2 \left(\frac{n\pi}{2} \frac{w_c}{h} \right). \end{aligned} \quad (13b)$$

Clearly CP1 and CP2 are determined by the channel geometry only. Table 2 and figure 1 show the values of CP1, CP2 and the ratio of CP2 to CP1 for channel aspect ratios between 0 (slot) and 1 (square) and allow these results to be used by others without recalculating CP1 and CP2.

If we integrate the separable equation (12) with respect to pressure (dp) and streamwise position (dz), the mass flow rate can be expressed as

$$\begin{aligned} \dot{m} &= \frac{w_c h^3}{R_s T \mu L} \frac{p_i^2 - p_o^2}{2} (-\text{CP1}) + \frac{w_c h^3}{R_s T \mu L} (p_i - p_o) \\ &\times \frac{2-\sigma}{\sigma} Kn_o p_o (-\text{CP2}) \\ &= \frac{w_c h^3 p_o^2}{2 R_s T \mu L} (-\text{CP1}) \left[\Pi^2 - 1 + 2 \frac{2-\sigma}{\sigma} Kn_o \frac{\text{CP2}}{\text{CP1}} (\Pi - 1) \right]. \end{aligned} \quad (14)$$

The zero-order term in the Knudsen number is due to the compressibility effect in the microchannels, while the first-order term is due to the velocity slip effect. In the limit of aspect ratio approaching zero this equation reduces to the mass flow rate formula

$$\dot{m} = \frac{2w_c h^3 p_o^2}{3R_s T \mu L} \left[\Pi^2 - 1 + 12 \frac{2-\sigma}{\sigma} Kn_o (\Pi - 1) \right] \quad (15)$$

for planar microchannels [3, 9].

The effect of velocity slip at the wall on the mass flow in the microchannels can be studied by dividing equation (14) by equation (14) with $Kn_o = 0$. The ratio is given by

$$\begin{aligned} \frac{\dot{m}_{\text{comp,s}}}{\dot{m}_{\text{comp,ns}}} &= 1 + 2 \frac{p_o}{p_i + p_o} \frac{2-\sigma}{\sigma} Kn_o \frac{\text{CP2}}{\text{CP1}} \\ &= 1 + \frac{2}{\Pi + 1} \frac{2-\sigma}{\sigma} Kn_o \frac{\text{CP2}}{\text{CP1}}. \end{aligned} \quad (16)$$

Table 2. Values of $-\text{CP1}$, $-\text{CP2}$ and the ratio of CP2 to CP1 with the channel aspect ratios.

a	0.000 002	0.02	0.20	0.365	0.40	0.60	0.80	1.00
$-\text{CP1}$	1.3333	1.3165	1.1653	1.0267	0.9975	0.8344	0.6869	0.5623
$-\text{CP2}$	8.0000	7.9189	7.1888	6.5215	6.3821	5.6311	5.0019	4.4985
CP2/CP1	6.0000	6.0150	6.1692	6.3520	6.3984	6.7482	7.2816	8.0000

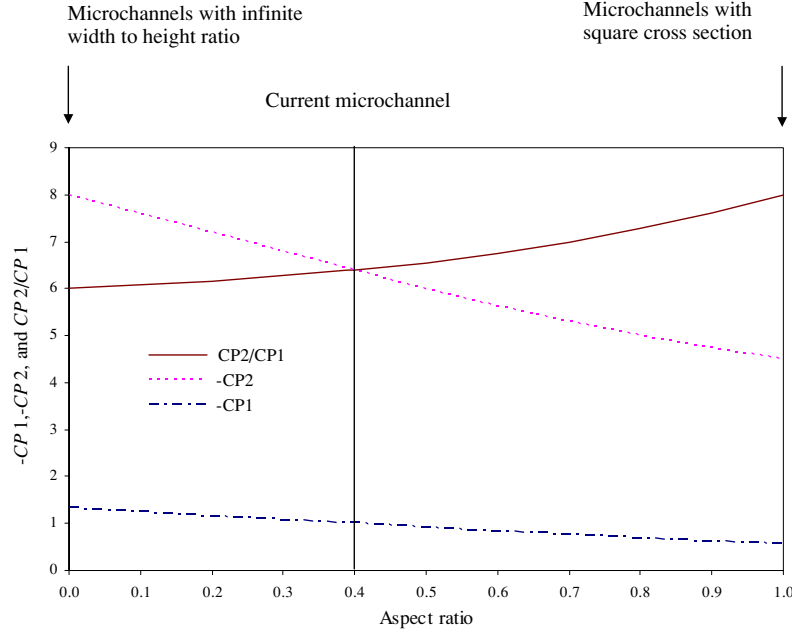


Figure 1. Values of $-CP1$, $-CP2$ and the $CP2$ to $CP1$ ratio as a function of the channel aspect ratios. (This figure is in colour only in the electronic version)

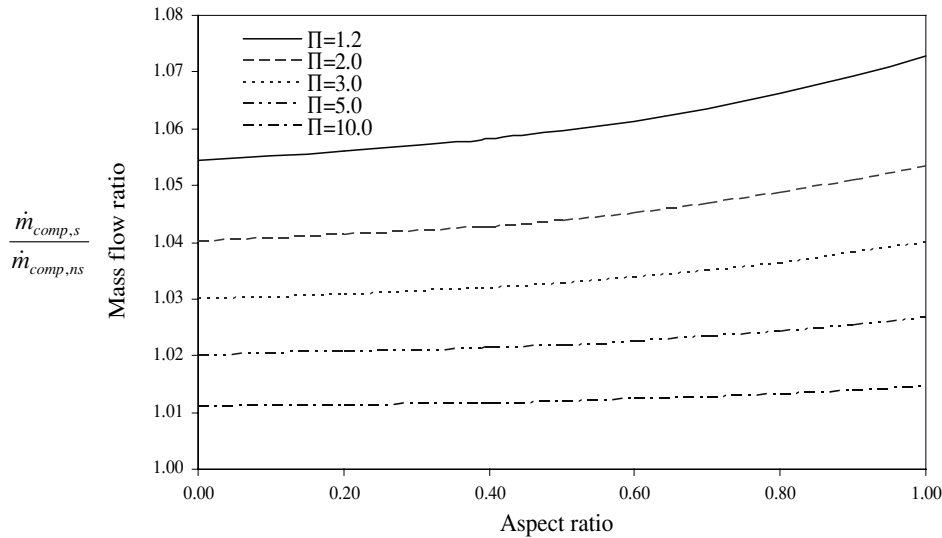


Figure 2. Mass flow rate increase due to velocity slip as a function of the channel aspect ratio at an outlet Knudsen number of 0.01 and a TMAC of 1.0.

Since Π is always greater than 1, σ is between 0 and 1, and the ratio $CP2/CP1$ is always positive, the velocity slip always increases the mass flow in a channel. For a particular channel aspect ratio, the velocity slip effect increases as the outlet Knudsen number increases and the inlet to outlet pressure ratio decreases. The same behavior has also been observed in planar microchannels [1]. Figure 2 shows the mass flow increase due to velocity slip for an outlet Knudsen number of 0.01 and a TMAC of 1.0. In this figure, mass flow rates increase due to the velocity slip as the channel aspect ratio increases from zero to unity while holding the outlet Knudsen number and pressure ratio constant.

Although many authors have used equation (15) for flows in thin, wide (but not planar) microchannels, this equation is

based on the assumption of the infinite width to height ratio. The reduction in the mass flow rate due to using the more accurate equation for flow in a rectangular channel can be written as

$$\frac{\dot{m}_{\text{slot}} - \dot{m}_{\text{rectangle}}}{\dot{m}_{\text{rectangle}}} = -1 + \frac{4}{3(-CP1)} \times \frac{[\Pi^2 - 1 + 12 \frac{2-\sigma}{\sigma} Kn_o(\Pi - 1)]}{[\Pi^2 - 1 + 2 \frac{2-\sigma}{\sigma} Kn_o \frac{CP2}{CP1}(\Pi - 1)]}. \quad (17)$$

The accuracy of using equation (15) depends on the aspect ratio, the pressure ratio, the TMAC and the Knudsen number. Figure 3 shows the relative differences of mass flow rates calculated from equation (17) for several different pressure ratios and Knudsen numbers. Clearly the differences increase

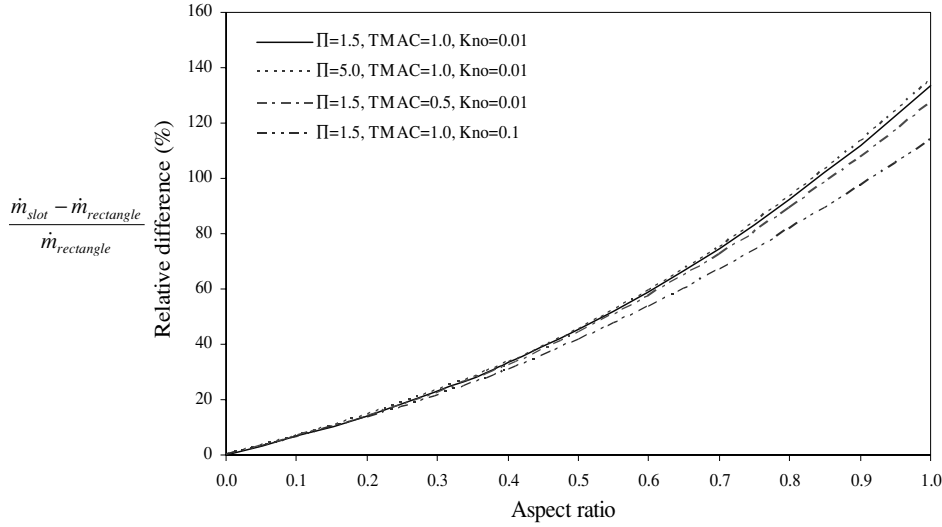


Figure 3. Relative differences of calculated mass flow rates with the current 2D model and 1D model as a function of the channel aspect ratios.

as the aspect ratio increases from zero to unity. Further, they increase with increasing pressure ratio, decreasing Knudsen number and increasing TMAC. For an aspect ratio of 0.03, used in the recent work [10], and the current aspect ratio of 0.39, the relative differences are 1.9% and 32.1% at an outlet Knudsen number of 0.01, a TMAC of 1.0 and a pressure ratio of 1.5, respectively.

2.3. Effective heights and TMAC

The third power dependence of the mass flow rate on the channel height implies that the calculation of mass flow rate is very sensitive to the channel size, especially to the smallest dimension, which we call the height here. Although we measured the heights of the microchannels used in these experiments with a profilometer, there are still geometric uncertainties—in particular the curved bottom surface resulting from the DRIE process [17]. For these reasons, it is usually advantageous and sometimes necessary to empirically extract the effective height of the microchannels from flow measurements. Because finding the effective height and TMAC using equation (14) directly is difficult due to its nonlinearity in the quantities of interest, equation (14) can be re-expressed as

$$\left(\frac{\dot{m}}{p_i - p_o}\right) = \frac{w_c h^3}{R_s T \mu L} (-CP1) \left\{ \frac{p_i + p_o}{2} \right\} + \frac{w_c h^3}{R_s T \mu L} \frac{2 - \sigma}{\sigma} Kn_o p_o (-CP2). \quad (18)$$

There is now a linear relationship between the mass flow conductance $\dot{m}/(p_i - p_o)$ and the average pressure in the channel $(p_i + p_o)/2$. The slope is $m1 = w_c h^3 (-CP1)/R_s T \mu L$ and the intercept is $b1 = w_c h^3 Kn_o p_o (-CP2)(2 - \sigma)/R_s T \mu L \sigma$. The height h can be extracted from the experimentally measured slope $m1$, as long as the other parameters in the slope are known, using

$$m1 \frac{R_s T \mu L}{w_c} = h^3 \left(-CP1 \left(\frac{h}{w_c} \right) \right). \quad (19)$$

Because CP1 is a power series with h inside a hyperbolic tangent function, no closed-form solution for h is possible. However, the height can easily be found iteratively with any numerical root finding technique.

Using a similar approach to find the TMAC, equation (14) can be modified as

$$\left(\frac{\dot{m}}{p_i^2 - p_o^2}\right) = \frac{w_c h^3}{2R_s T \mu L} (-CP1) + \frac{w_c h^3}{2R_s T \mu L} \frac{2 - \sigma}{\sigma} Kn_o p_o (-CP2) \left\{ \frac{2}{p_i + p_o} \right\}, \quad (20)$$

where $\dot{m}/(p_i^2 - p_o^2)$ is a linear function of the inverse of the average pressure in which the slope is $m2 = w_c h^3 Kn_o p_o (CP2)(2 - \sigma)/2R_s T \mu L \sigma$ and the intercept is $b2 = w_c h^3 (-CP1)/2R_s T \mu L$. The TMAC can be obtained from the slope $m2$ by the following expression:

$$m2 \frac{2R_s T \mu L}{w_c h^3 Kn_o p_o (-CP2)} = \frac{2 - \sigma}{\sigma} \quad (21)$$

after the height is obtained from equation (19) above. Unlike equation (19), this expression need not be iterated because CP2 depends only on h and w_c , both of which are already known.

2.4. TMAC calculation for non-homogeneous microchannels

It is most straightforward to measure the TMAC in a channel whose all sides are the same—material as well as surface finish. However, microchannels are often composed of several materials, such as the glass and silicon used here. Further, even walls of the same material may have different surface finishes, such as the much rougher side than bottom walls in DRIE channels. Consequently, the TMACs extracted from equation (21) represent averaged values for the material-surface finish combination. When the TMACs for the top and bottom walls in a parallel-plate (aspect ratio = 0) channel are different, the velocity can be represented as

$$v = \frac{h^2}{2\mu} \left(-\frac{dp}{dz} \right) \left[1 - \left(\frac{y}{h} \right)^2 + \frac{2(A - B)Kn}{(1 + (A + B)Kn)} \frac{y}{h} + 4B \cdot Kn + \frac{2(A - B)Kn(1 + 2B \cdot Kn)}{(1 + (A + B)Kn)} \right], \quad (22)$$

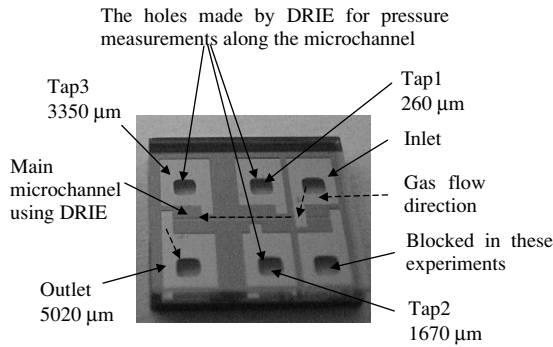


Figure 4. Schematic of the rectangular microchannel chip using DRIE and anodic bonding.

where A and B represent the quantity $(2 - \sigma)/\sigma$ computed on the top and bottom wall, respectively. According to conservation of mass, the mass flow rate found using the effective TMAC must be equal to that considering the differing TMACs, equation (22), integrated across the channel cross section. There are an insufficient number of equations to find both A and B . However, if the TMAC of one surface is known from a previous experiment, the TMAC of the other surface can be found by equating the two mass flow rates and solving for the unknown TMAC according to

$$A = \frac{2C(1 + B \cdot Kn) - B}{(1 - 2C \cdot Kn + 4B \cdot Kn)}, \quad (23)$$

where C is $(2 - \sigma)/\sigma$ computed with the measured average TMAC, and B is known from another experiment.

This derivation can be extended to the general rectangular channel cases—four different materials and surface finishes. The symmetry boundary conditions, equations (5a) and (5c), cannot be used in these cases. In fact, these two boundary conditions must be replaced with velocity slip boundary conditions at the boundaries ($x = -w_c$ and $y = -h$). Further, since the TMACs on the surrounding walls can be different, we might have four different velocity slip boundary conditions. The mass flow rate using the velocity obtained from these four different boundary conditions is equated with that using the effective velocity obtained from all the same velocity slip boundary conditions. Then, the formula for extracting the TMAC on a single wall in a rectangular microchannel can be found as we obtain equation (23). More detailed derivations will be available in another paper in the near future.

2.5. Microchannel fabrication and experimental setup

The microchannel chip ($8.1 \times 8.1 \text{ mm}^2$) consists of the main microchannel, inlet/outlet reservoirs and five reservoirs for measuring pressure along the main microchannel (figure 4). The fabrication procedure is straightforward as shown in figure 5. We begin with $525 \mu\text{m}$ thick P-type (100) 4 inch silicon wafers. Initially $0.6 \mu\text{m}$ thick thermal oxide is grown on both sides. The microchannels and pressure measurement reservoirs on the front side are made by the DRIE process at Cornell University. The wafers are oxidized again and the backside is etched through the wafers to the bottom surfaces of the reservoirs, connecting the inlet and outlet reservoirs to the backside of the chip where the tubes are epoxy bonded to

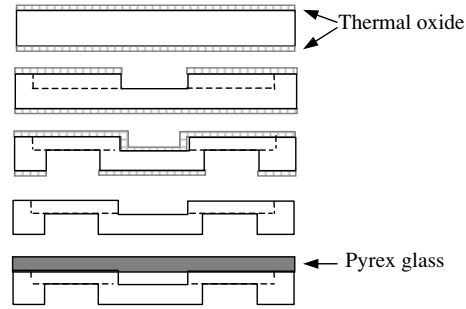


Figure 5. Fabrication procedure of the rectangular microchannel chip using DRIE and anodic bonding.

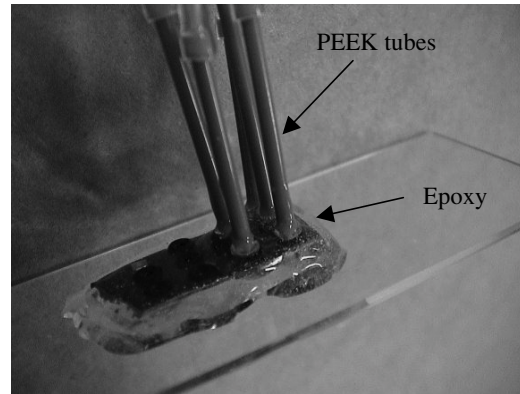


Figure 6. Photograph of the chips with PEEK tubes connected and sealed using epoxy.

Table 3. Average roughness (Ra) of each side of the microchannels.

Top surface of the microchannels (Pyrex no. 7740)	2.0 nm (manufacturer's datasheet)
The bottom surface of the microchannels	6.43 nm
Sidewalls of the microchannels	<30 nm [24]

supply and remove flow. Finally, anodic bonding is done with 1 mm thick Pyrex 7740 glass wafers at $350 \text{ }^\circ\text{C}$ and 1000 V, and the bonded wafers are diced.

Figure 6 shows the chip assembly with five tubes connected using an epoxy (5 Minute[®] Epoxy, Devcon). This epoxy, intended to bond metals, ceramics and glasses, has a good gap filling capacity and is transparent when cured at room temperature. The 0.55 mm inner diameter PEEK tubes are placed in the five holes on the backside of the chip with O-rings used to stabilize them. The remaining hole is blocked. The epoxy is then applied and cured for 12 h, the full cure time according to its datasheet.

Table 3 shows the average roughness (Ra) of the various surfaces of the microchannel walls. The roughness of the bottom silicon surface created by the DRIE process is measured with a profilometer (Tencor Alpha-step 200). It has an average surface roughness of 6.43 nm. Additionally, the root mean square roughness of the sidewall, also created by DRIE, is reported to be less than 30.0 nm [24]. Direct measurements of the sidewall roughness are not done because of the difficulty in accessing those regions. The Pyrex glass has an average roughness of less than 2.0 nm according to the manufacturer's datasheet (Sensor Prep Services Inc., USA).

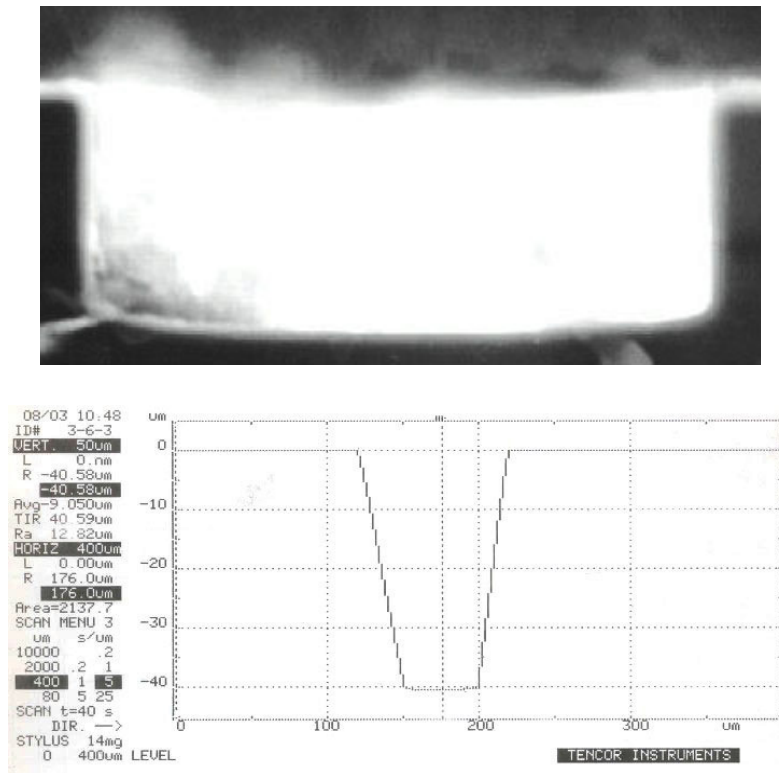


Figure 7. A scanning electron micrograph of the cross section of the microchannel (top) and the profile measurement (bottom).

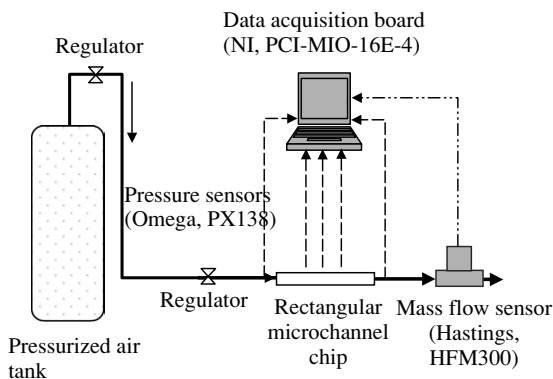


Figure 8. Experimental setup for pressure and flow measurements.

Figure 7 shows a scanning electron micrograph (400×) of the cross section of the main microchannel. The bottom surface appears slightly curved, which is a general feature of the DRIE process [17]. The channel heights are measured with a profilometer and the widths are measured with an optical microscope (Nikon TE200 with 40× objective). The channel height at the center of the channel bottom, the deepest location, is 40.53 μm with a standard deviation of 0.03 μm and the channel width is 100.86 μm with a standard deviation of 0.66 μm. The aspect ratio of the microchannel is 0.40 based on the largest height.

Figure 8 shows the experimental setup. It consists of a compressed gas cylinder, regulators, commercial pressure sensors, and a commercial mass flow sensor, a data acquisition board and the microchannel chip. Air (CGA grade D) is used

as the working fluid. The pressure sensors (Omega PX138) available for differential pressure measurements have a typical accuracy of ±0.1% FS, where the FS is a gauge pressure of 103.4 kPa. The flow sensor (Hastings, HFM300) has an accuracy of ±0.75% FS at 3σ_S, where the FS is 5 sccm (1.077 × 10⁻⁷ kg s⁻¹). The data acquisition board (NI PCI-MIO-16E-4) is connected to a computer and is used to take continuous and simultaneous measurements of flow rates and pressures. The ambient temperature and pressure are measured with a T-type thermocouple and a mercury barometer, respectively.

Before beginning experiments, the mass flow sensor is calibrated with a high-precision flow sensor (IGFS 1097-06 at ATC, Inc.). To determine whether the system has any leaks, in two experiments the mass flow sensor is placed first immediately before and then immediately after the chip assembly with the exit to the ambient blocked. The flow rates due to a gauge pressure of 22.89 kPa higher than the highest inlet pressure used in the experiments are measured in both cases. The maximum measured leak rate is 0.0034 sccm (7.322 × 10⁻¹¹ kg s⁻¹), which is 0.07% of the highest flow rate in the experiments and is within the manufacturer's specifications of the accuracy of the mass flow sensor.

Compressed air is passed through a pressure regulator and a needle valve to control the pressure and flow rate and then applied to the inlet of the microchannel while the outlet is held at ambient pressure. At steady-state conditions the differential pressure (relative to ambient) at each reservoir along the microchannel is acquired by the data acquisition board along with the mass flow rate through the microchannel for 4 min at 2 Hz. The differential pressure between the first and the third reservoirs is also acquired.

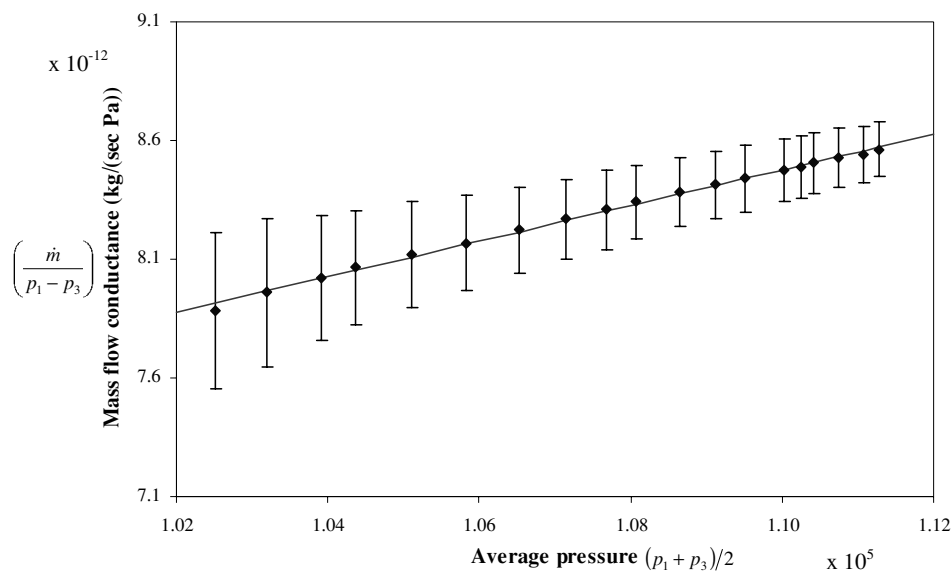
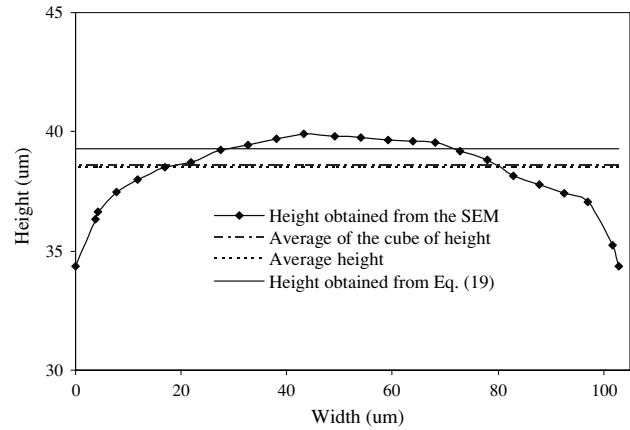
Table 4. Experimental conditions and physical properties of air.

Parameter	Range or mean values
Ambient pressure (p_a)	98 482 Pa
The first tap to the third tap pressure ratio	1.0028–1.0998
Mean free path of air at the outlet (λ)	67.97 nm
Outlet Knudsen number of air (Kn_o)	0.0017
Temperature (T)	297 K
Molecular mass of air (g mol^{-1})	28.96
Outlet Mach number (Ma_o)	0.0014–0.0604
Reynolds number (Re)	1.3–52.7
Reynolds number (Re_{D_h})	1.8–75.9
Ratio of specific heats (γ)	1.4

3. Results and discussion

Table 4 summarizes the experimental conditions and physical properties of air. A hard sphere model is used to calculate the effective molecular diameter and the mean free path [2]. For realistic molecules, a cutoff distance between molecules is arbitrarily determined, and it is difficult to define the molecular diameter and mean free path. The hard sphere model is the conventional solution to this problem and is commonly used despite the fact that it is reported to be slightly different from real gases [25].

Figure 9 shows the mass flow conductance as a function of the average pressure of the first pressure tap and the third pressure tap, which were used to avoid inlet and exit pressure drops that exist for higher Reynolds numbers. The error bars indicate 95% confidence intervals. Mass flow conductance is defined as the mass flow rate divided by the pressure difference. The distance of $260 \mu\text{m}$ from the inlet to the first tap is larger than the largest expected entrance lengths of $243 \mu\text{m}$ [26] and $129 \mu\text{m}$ [21] based on the hydraulic diameter of the channel. Entrance length was also measured in water flows using micro particle image velocimetry (μPIV) at a Reynolds number of 5.1–77.0 based on the hydraulic diameter. At the largest


Figure 9. Mass flow conductance versus the average of the first tap pressure and the third tap pressure, where the slope is used to extract the effective height.

Figure 10. Height of the bottom surface versus the width of the microchannel.

Reynolds number of 77.0, the entrance length was measured to be $134 \mu\text{m}$. From this result, the entrance length at the highest Reynolds number in gas flow measurements is expected not to exceed the first pressure tap location.

Equation (19) was used to extract the effective channel height from the slope of figure 9. The effective height is computed to be $39.27 \mu\text{m}$, which is somewhat smaller than the largest height ($40.53 \mu\text{m}$) measured with the profilometer. This difference is due to the curved bottom surface of the channel cross section shown in the SEM in figure 7. Other effective heights can be obtained from the SEM image. Figure 10 shows the distance between the curved bottom and flat top wall, i.e. channel height $h(x)$, as a function of the width position x . The solid line indicates the effective height obtained by the measurement slope and equation (19). The dashed line indicates the mean height and the dot-dashed line indicates the mean of the cube of height, a quantity that reflects the cubic dependence of equation (14) on height.

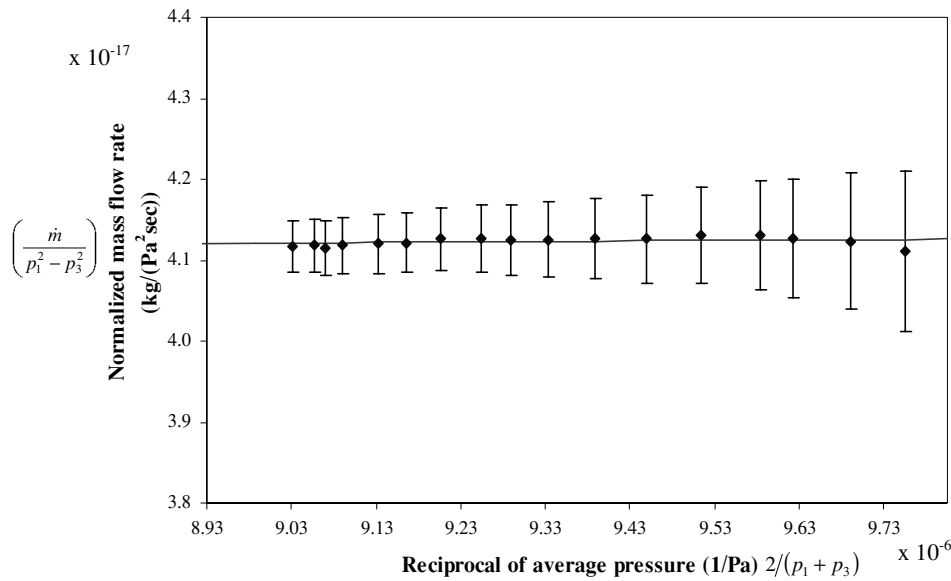


Figure 11. Normalized mass flow rate versus the reciprocal of the average pressure of the first and third taps, where the slope is used to find the effective TMAC.

Table 5. Effective height measurements using three different methods.

Method	Range of effective heights (μm)
Equation (19) and flow measurements	38.84–39.70
Average height	37.86–39.32
Average of the cube of height	37.90–39.36

Table 5 shows the range of the effective heights obtained from three methods. These three effective heights are overlapped within their uncertainties. The relative differences among the three effective perimeters of the cross section relative to the measured perimeter from the SEM image are less than 2%, which satisfies our physical intuition. The effective height from the flow measurements and equation (19) can cover the curvature effect of the bottom surface on the mass flow rate. It should be noted that the height extracted from equation (19) does not depend on the TMAC.

Figure 11 shows the normalized mass flow rate as a function of the reciprocal of the average pressure of the first pressure tap and the third pressure tap. The TMAC for air in this channel was obtained as 0.85 from the slope of figure 11 using equation (21). Other researchers have experimentally observed TMACs to be between 0.2 and 1.0 [1, 5]. The lower limit is for exceptionally smooth surfaces while the upper limit is typical of many practical surfaces [1]. Further, TMAC values can vary with surface roughness by about 15% for the same surface material [27]. Table 6 shows the TMACs of several gases and surfaces. The TMAC for the case of air flowing through a channel made of smooth Pyrex glass and DRIE-etched silicon has not been available. This value of 0.85 is somewhat smaller than 0.93 obtained in nitrogen flowing in a glass/silicon channel made by DRIE [16]. The difference between these TMAC values may be attributed to the different gases used. It should be noted that the TMAC value reported here is an average value for the several materials

Table 6. Range of the TMACs of several gases and surfaces [1, 3, 29].

Gas	Surface material	TMAC range
Air	Aluminum	0.87–0.97
Air	Iron	0.87–0.93
Air	Bronze	0.88–0.95
Helium	Polished copper	0.65–0.95
Helium	Glass	0.70–0.80
Nitrogen	Silicon	0.81–0.95
Argon	Silicon	0.65–0.98

and surface finishes comprising the channel, so the average TMAC can be less than unity although the TMACs on some surfaces comprising a channel are approximately unity. In fact, according to equation (23), the TMAC on the top wall is obtained as 0.90 when the TMAC on the bottom wall is unity and the average TMAC is 0.95 at $Kn = 0.01$. This should be true for rectangular channels. In the current channel, TMACs could be unity on the side walls, the roughest walls, and the top wall is very smooth glass whose TMAC should be smaller than unity. We can conclude that the average TMAC should be less than the TMACs on the side walls and larger than the TMAC on the top wall. It should be noted here that the obtained average TMAC of 0.85 is less than the TMAC of 0.89 for glass and air in [28]. The TMAC of this reference was obtained from viscosity measurements in glass capillaries by Warburg in the 1870s [28]. The possible reasons for this discrepancy include uncertainties of the current measurement and different surface roughnesses of the glasses used. In fact, the TMAC of 0.89 is within the standard deviation of the current measurement. Also, the surface roughnesses of the capillaries were not available while the current Pyrex glass has an average roughness of 2 nm. Using the approaches in this work, a more complicated expression for the TMACs of all the walls in a rectangular channel can be developed.

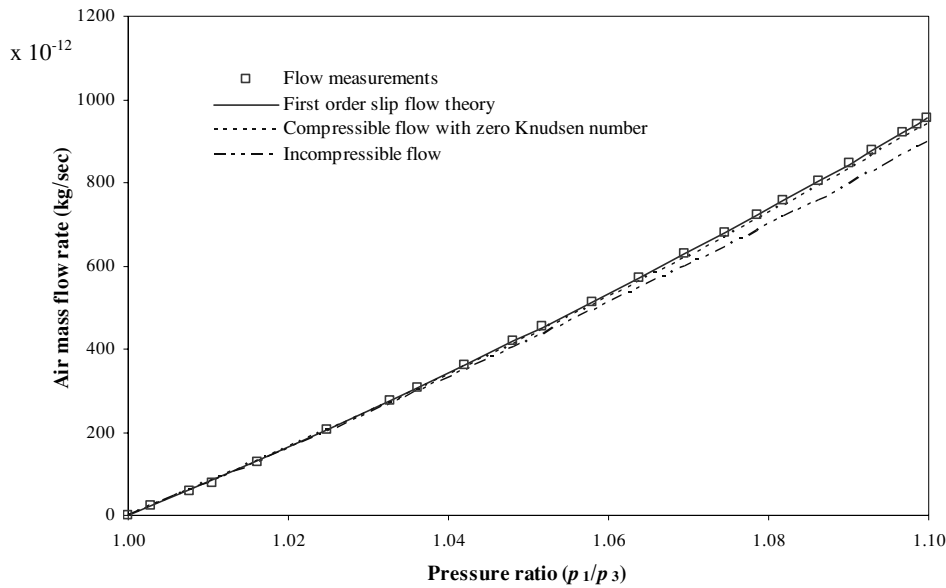


Figure 12. Air mass flow rate as a function of the first tap to third tap pressure ratio. The 95% confidence intervals of the mass flow measurements are within 0.70% of the measured maximum mass flow rate and hence are not plotted here because they would be too small to be seen.

Figure 12 shows the measured mass flow rates as a function of the ratio of the first tap pressure to the third tap pressure. The square symbols represent the readings of the mass flow sensor while the solid line is from the analytical expression of equation (14) using the effective height and the extracted TMAC above. The 95% confidence intervals of the mass flow measurements are within 0.70% of the measured maximum mass flow rate. There is close agreement between the measurements and the calculation by the slip flow formula. The experimental data are closely fitted with the effective height and average TMAC. The dashed line indicates equation (14) with the outlet Knudsen number of zero (compressible flow only) while the dot-dot-dashed line indicates prediction by the incompressible no-slip flow model.

4. Conclusions

We have presented analytical expressions of the mass flow rate in a rectangular channel in the slip flow regime. These expressions were derived in a different way from others [1, 20–22] and reduce to the expression of Arkilic *et al* [3, 9] as the aspect ratio approaches zero, the parallel plate case. Using those expressions, we also presented effective heights and TMACs of air flowing in a rectangular microchannel fabricated by DRIE. The microchannel chips were made by DRIE and anodic bonding, causing a slightly curved channel bottom. Consequently, the effective channel height was extracted from the experimental mass flow rate versus pressure drop behavior using our new equations. The extracted effective height of the channel is $39.27 \mu\text{m}$, which is slightly less than the measured largest height of $40.53 \mu\text{m}$. This difference is due to the curved bottom surface of the channel cross section. Three effective heights were obtained from different methods and they were within their uncertainties. We can conclude that the effective height from flow measurements can cover the

curvature effect of the bottom surface on mass flow rate. We extracted the TMAC of 0.85 for air in these channels under atmospheric conditions. This TMAC value is an average value for the channels which are made of Si/glass and different surface finishes. The average TMAC should be in between the TMACs (the largest value) on the side walls and the TMAC (the smallest value) on the top wall.

Acknowledgments

This work was supported by the Indiana 21st Century Research and Technology Fund. We are grateful to Yabin Zhao for his helpful discussions.

References

- [1] Karniadakis G E and Beskok A 2002 *Micro Flows: Fundamentals and Simulation* (Berlin: Springer)
- [2] Harley J C, Huang Y, Bau H H and Zemel J N 1995 Gas flow in micro-channels *J. Fluid Mech.* **284** 257
- [3] Arkilic E B, Breuer K S and Schmidt M A 2001 Mass flow and tangential momentum accommodation in silicon micromachined channels *J. Fluid Mech.* **437** 29
- [4] Zohar Y, Lee S Y K, Lee W Y, Jiang L and Tong P 2002 Subsonic gas flow in a straight and uniform microchannel *J. Fluid Mech.* **472** 125
- [5] Gad-el-Hak M 1999 The fluid mechanics of microdevices—the freemann scholar lecture *J. Fluids Eng.* **121** 5
- [6] Kennard E H 1938 *Kinetic Theory of Gases* (New York: McGraw-Hill)
- [7] Goodman F O and Wachman M A 1976 *Dynamics of Gas-Surface Scattering* (New York: Academic)
- [8] Maxwell J C 1965 *The Scientific Papers of James Clerk Maxwell* (New York: Dover)
- [9] Arkilic E B, Schmidt M A and Breuer K S 1997 Gaseous slip flow in long microchannels *J. Microelectromech. Syst.* **6** 167
- [10] Pong K C, Ho C M, Liu J and Tai Y C 1994 Non-linear pressure distribution in uniform microchannels *ASME FED-197* 51

- [11] Pfahler J, Harley J C, Bau H and Zemel J N 1991 Gas and liquid flow in small channels *ASME DSC-32* 49
- [12] Liu J, Tai Y C and Ho C M 1995 MEMS for pressure distribution studies of gases flows in microchannels *IEEE MEMS 1995* p 209
- [13] Shih J C, Ho C M, Liu J and Tai Y C 1996 Monatomic and polyatomic gas flow through uniform microchannels *ASME DSC-59* 197
- [14] Lee S Y K, Wong M and Zohar Y 2001 Gas flow in microchannels with bends *J. Micromech. Microeng.* **11** 635
- [15] Li X, Lee W Y, Wong M and Zohar Y 2000 Gas flow in constriction microdevices *Sensors Actuators A* **83** 277
- [16] Colin S, Lalonde P and Caen R 2004 Validation of a second-order slip flow model in rectangular microchannels *Heat Transfer Eng.* **25** 23
- [17] Ayon A A, Zhang X and Khanna R 2000 Ultra deep anisotropic silicon trenches using deep reactive ion etching (DRIE) *Solid-State Sensor and Actuator Workshop Hilton Head* p 339
- [18] Maurer J, Tabeling P, Joseph P and Willaime H 2003 Second-order slip laws in microchannels for helium and nitrogen *Phys. Fluids* **15** 2613
- [19] Arkilic E B, Schmidt M A and Breuer K S 1996 TMAC measurement in silicon micromachined channels *Proc. Symp. on Rarefied Gas Dynamics (Beijing, China, August 1996)* pp 1–5
- [20] Aubert C and Colin S 2000 High-order boundary conditions for gaseous flows in rectangular microchannels *Microscale Thermophys. Eng.* **5** 41
- [21] Morini G L and Spiga M 1998 Slip flow in rectangular microtubes *Microscale Thermophys. Eng.* **2** 273
- [22] Sharipov F 1999 Non-isothermal gas flow through rectangular microchannels *J. Micromech. Microeng.* **9** 394
- [23] Ebert W A and Sparrow E M 1965 Slip flow in rectangular and annular ducts *J. Basic Eng.* **87** 1018
- [24] Chabloz M, Sasaki Y, Matsuura T and Tsutsumi K 2000 Improvement of sidewall roughness in deep silicon etching *Microsyst. Technol.* **6** 86
- [25] Bird G A 1983 Definition of mean free path for real gases *Phys. Fluids* **26** 3222
- [26] Shah R K and London A L 1978 Laminar Flow Forced Convection in Ducts *Advances in Heat Transfer Series* (New York: Academic)
- [27] Thomas L B and Lord R G 1974 Comparative measurements of tangential momentum and thermal accommodations on polished and on roughened steel spheres *Proc. Int. Symp. on Rarefied Gas Dynamics* pp 405–12
- [28] Millikan R A 1923 Coefficients of slip in gases and the law of reflection of molecules from the surfaces of solids and liquids *Phys. Rev.* **21** 217
- [29] Seidl M and Steinheil E 1974 Measurement of momentum accommodation coefficients on surfaces characterized by Auger spectroscopy, SIMS and LEED *Proc. Int. Symp. on Rarefied Gas Dynamics* pp E9-1–E9-12